Quantification of evaporation induced error in atom probe tomography using molecular dynamics simulation

*Shu Jian Chen, Xupei Yao, Changxi Zheng, Wen Hui Duan**

Department of Civil Engineering, Monash University, Clayton, VIC 3800, Australia

Abstract

Non-equilibrium molecular dynamics was used to simulate the dynamics of atoms at the atom probe surface and five objective functions were used to quantify errors. The results suggested that before ionization, thermal vibration and collision caused the atoms to displace up to 1 Å and 25 Å respectively. The average atom displacements were found to vary between 0.2 and 0.5 Å. About 9 to 17% of the atoms were affected by collision. Due to the effects of collision and ion-ion repulsion, the back-calculated positions were on average 0.3–0.5 Å different from the pre-ionized positions of the atoms when the number of ions generated per pulse was minimal. This difference could increase up to 8–10 Å when 1.5 ion/nm^2 were evaporated per pulse. On the basis of the results, surface ion density was considered an important factor that needed to be controlled to minimize error in the evaporation process.

Keywords

Evaporation; Atom probe; Aluminum; Reconstruction; Molecular dynamics

1. Introduction

Atom probe tomography (APT) is a high-resolution characterization tool providing 3D elemental distribution in materials. With the use of a strong electric field [1] or laser pulse [2], [3], the atoms of a sharpened sample tip with diameter in the range 50–110 nm [4], [5] can be evaporated layer by layer, and the evaporated ions are detected by a microchannel plate (MCP) detector [6]. Time-of-flight mass spectrometry [7], [8] is then used to identify atom species and calculate their positions in three dimensions [9]. During the APT process, sample evaporation occurs layer by layer, providing 3D resolution of the sample. By magnification of a highly curved electric field, the resolution of APT can often reach less than 0.3 nm [10], [11].

Over the years, APT has been widely used to investigate a broad spectrum of materials including metals [12], [13], ceramics [14], [15], [16], polymers [17], [18], and biomaterials [19], [20]. Specimens that have good electrical conductivity, such as metals, have been the favorite subjects of investigation using voltage-pulsed field (10 and 60 V/nm for most metal) [21], [22] evaporation. For example, APT examination of pure metals and multicomponent engineering alloys, such as shape memory alloy and aerospace alloy [23], [24], [25], has revealed the effect of precipitates on the superelastic response of FeMnAlNi alloy under compression. Furthermore, APT has been used to study ceramic nanocomposites [26] and oxide ceramics [27], and the microstructure of bulk polycrystalline Al_2O_3 was discovered [28]. APT has been also used to identify the oxidation process of conducting polypyrrole in conductive polymers [17]. More interestingly, researchers in biology have used APT to obtain the chemical tomography of buried organic-inorganic interfaces in chiton tooth [20].

However, as the position of every atom in the sample is obtained by back-calculation via theoretical models [1] based on their position detected on the detector [1], [8] and time-flight mass spectrometry [11], the model for the APT process is critical for accurate reconstruction of the sample atomic structure. The projection of ions from specimen to a location-sensitive detector, as indicated in Fig. 1(a), can be divided into three processes, namely ionization, evaporation, and flight [11]. A study of dielectric material has used a FEM/continuum Poisson equation to simulate the potential distribution and the atom position based on a theoretical model of the electric field and the mass-to-charge ratio [29]. FEM/continuum simulation has been used in a number of studies of the effect of electric strength, specimen geometry, and distance between specimen and detector on reconstruction accuracy during the flight process [29], [30]. Quantum mechanics and density function theory have been used to investigate the ionization of MgO under APT [31]. The study of the ionization provides information on the type of ions generated and the decomposition process of the sample under an electric field [1], [4] or laser pulse [2], [32].

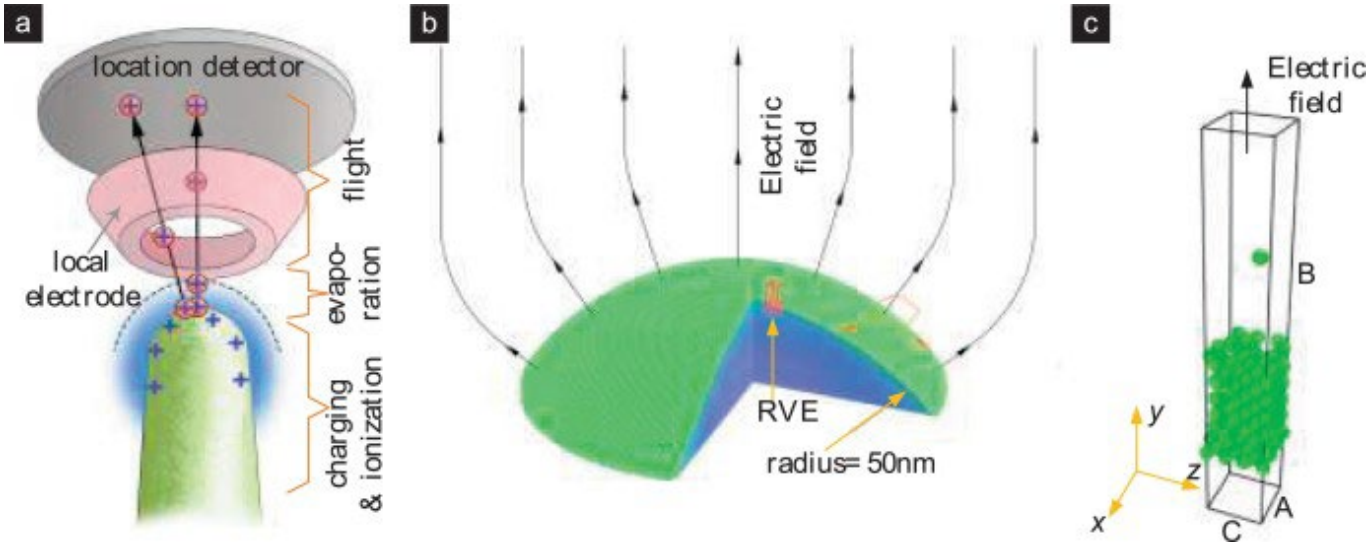

Fig. 1. (a) schematics of the whole atom probe proces, (b) zoomed in for evaporation, c) representative model used in this study.

The evaporation process at the sample surface during APT has rarely been investigated quantitatively. To avoid confusion, in this study, the term “evaporation process” refers to the movement of atoms after ionization but before leaving the surface. An ion is deemed to have left the surface when its distance from the surface is sufficiently great. Thus, the force (excluding the force due to the electric field) between the atom and the surface [33], [34] becomes negligible. This distance is often between 10 and 15 Å [35]. It is proposed here that non-equilibrium molecular dynamics (MD) simulation can be used to investigate the evaporation process of atoms in APT. Studies [36] have demonstrated that MD is an efficient tool for studying the interaction between atoms and surface.

Herein, non-equilibrium MD [37] is used to simulate the atomic scale evaporation process of APT of Al-based metallic material. The main source of error is identified and quantified, pointing to the evaporation process. The errors include disturbance of the atomic structure, disturbance of the flight path of atoms due to atom collision,

thermal vibration, and van der Waals attraction of the evaporated atoms. Five objective functions are proposed to quantitatively represent the error due to the evaporation process. By using the new simulation scheme and the objective functions, the effects of various ion densities and electrical field strengths are evaluated. This study provides better understanding of the evaporation process, which is beneficial for optimizing experimental parameters and improving the back-computation accuracy of APT.

2. Method

Fig. 1(b) shows a small portion of an atom probe tip with a radius of 50 nm. Based on the principles of electrostatic equilibrium [38], the direction of the electric field is perpendicular to the surface of the specimen tip, as shown in Fig. 1(b). A small cuboid volume is taken from the surface of the tip as a representative volume element (RVE) of the probe surface. An atomic model of the RVE is shown in Fig. 1(c). The block of Al and Cr atoms (Fig. 1(c)) with the dimensions 22 × 12.48 × 12.48 Å in the *y, x*, and *z* directions was built in a periodic box and the ratio of the number of aluminum to chromium atoms is about 10:1. Since the modeling size of the block of atoms in the RVE is small compared to the diameter of a real probe (1000 Å), a rectangular cuboid RVE can be used to represent the actual quadrilateral frustum RVE (Fig. 1(b)) without significant error. Because a small RVE is used, the electrical field in the *y* direction can be treated as uniform, as illustrated in Fig. 1(c).

Relaxation of the structure is achieved by an initial geometry optimization process (using the conjugate-gradient method), followed by a canonical ensemble (*i.e.*, constant volume and constant temperature dynamics) at 70 K for 50 ps. After relaxation, the non-equilibrium MD begins simulating the ion density. Then the cations including Al^{2+}, Al^{3+}, and Cr^{2+} with a Al^{2+} to Al^{3+} ratio of 4:1 [39] are evaporated and flied under an applied electric field based on a microcanonical ensemble (*i.e.*, constant volume and constant energy dynamics). Every 0.015 ps, the atoms that are about 20–30 Å away from the surface are removed from the system. After all the charged atoms generated during this pulse are removed, cations are considered to have escaped from the main body of the sample alloy and the evaporation stage ends. Because the atom leaves the surface in the very short time of 0.090 ps, no cooling of the atoms is applied during this period.

Before the application of the next pulse, however, the samples needs to be cooled and in APT, liquid nitrogen is used to cool the sample [40]. In the cooling process, the bottom layers of the sample alloy are used as a cooler to simulate the cooling of the sample using liquid nitrogen [1]. On the basis of a microcanonical ensemble, thermal energy is extracted from the system via the cooler to gradually cool the atoms. For every 0.83 ps, the temperature of the atoms in the cooler is adjusted to 70 K by velocity scaling using

$$v_{i.,new} = \sqrt{\frac{T_0}{T_{ins\,tan}}} v_{i,old} \quad (1)$$

where T_0 is the target temperature, T_{instan} the instantaneous temperature, and adjustment of temperature is defined as

$$u_t = T_0 - T_{instan} \quad (2)$$

The atomic interaction is simulated by the COMPASS force field (condensed-phased optimized molecular potential for atomistic simulation studies) [41], [42]. The properties of aluminum and chromium have been proved to be properly described by this force field [35], [43], [44].

3. Results and discussion

3.1. Disturbance of pre-ionization atomic structure

The evaporation process can introduce two main types of error, the first of which is disturbance of the pre-ionized atomic structure due to the evaporation of atoms. To permit a clear view of the behavior of the atoms, the simulated evaporation process is examined in unwrapped views. Fig. 2 demonstrates the unwrapped *x*-*y* and *z*-*y* views used in this study. As shown in Fig. 2, each layer of atoms in the *x* or *z* directions is placed as an array with minimal overlapping. The benefit of using an unwrapped view compared to the traditional cross-section view or 3D model view is that the unwrapped view allows the viewing of each atom with minimal obstruction from the atoms in front of or behind it. Using an unwrapped view permits better examination of each atom in the system.

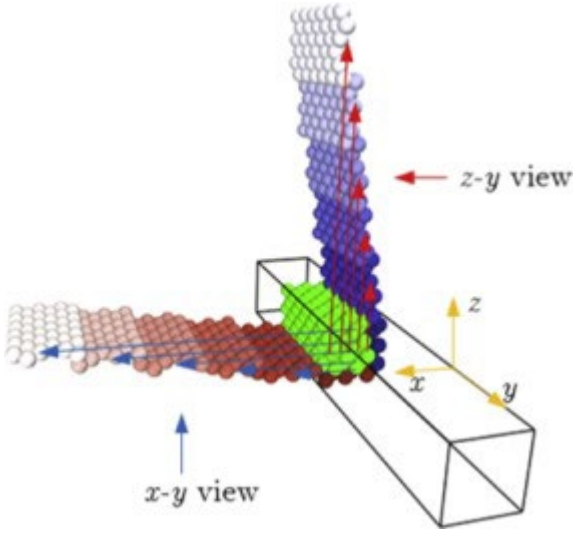

Fig. 2. Unwrapped *x-y* and *z-y* views by expanding layers of atoms in *x* and *z* directions respectively. These unwrapped views allow the position, force, and velocity of each layer of atoms to be shown on 2D graphs without being obscured.

Fig. 3 shows *x-y* and *z-y* unwrapped views of the RVE during the evaporation of Al and Cr atoms from an alloy block under a field strength of 136.0 V/nm. In this case, the atoms are evaporated one by one. The entire evaporation processes for different field strengths and surface ion densities are available in the Supplementary materials. Fig. 3 demonstrates that, under a strong electric field, a charged atom flying away from the surface of the probe can cause three main types of disturbance of the original atomic structure of the sample. As shown in Fig. 3(a), charged atoms on the top layer may collide with a non-charged atom at the surface, causing the non-charged atom to be knocked away from its original position. The knocked atom may fly away from the surface or bounce on the surface, as shown in Fig. 3(b). This knock event not only disturbs the non-charged atoms but also biases the direction of the force vector on the charged atom from the direction of *E* (as shown in Fig. 3(a) and (b)). The effect on the charged atom is discussed in Section 3.2. Another type of disturbance is that the flying away of charged atoms agitates the vibration of the atoms at the surface, causing the temperature of the top surface to increase. As shown in Fig. 3(a)–(f), there are generally more high-temperature atoms (light colored) at the top layers. The third type of disturbance is due to the van der Waals attraction [45] of the evaporated atom that can create an significant upward force on a nearby atom when overlapped with the vibrational force of the nearby atom (as shown in Fig. 3(e) and (f)).

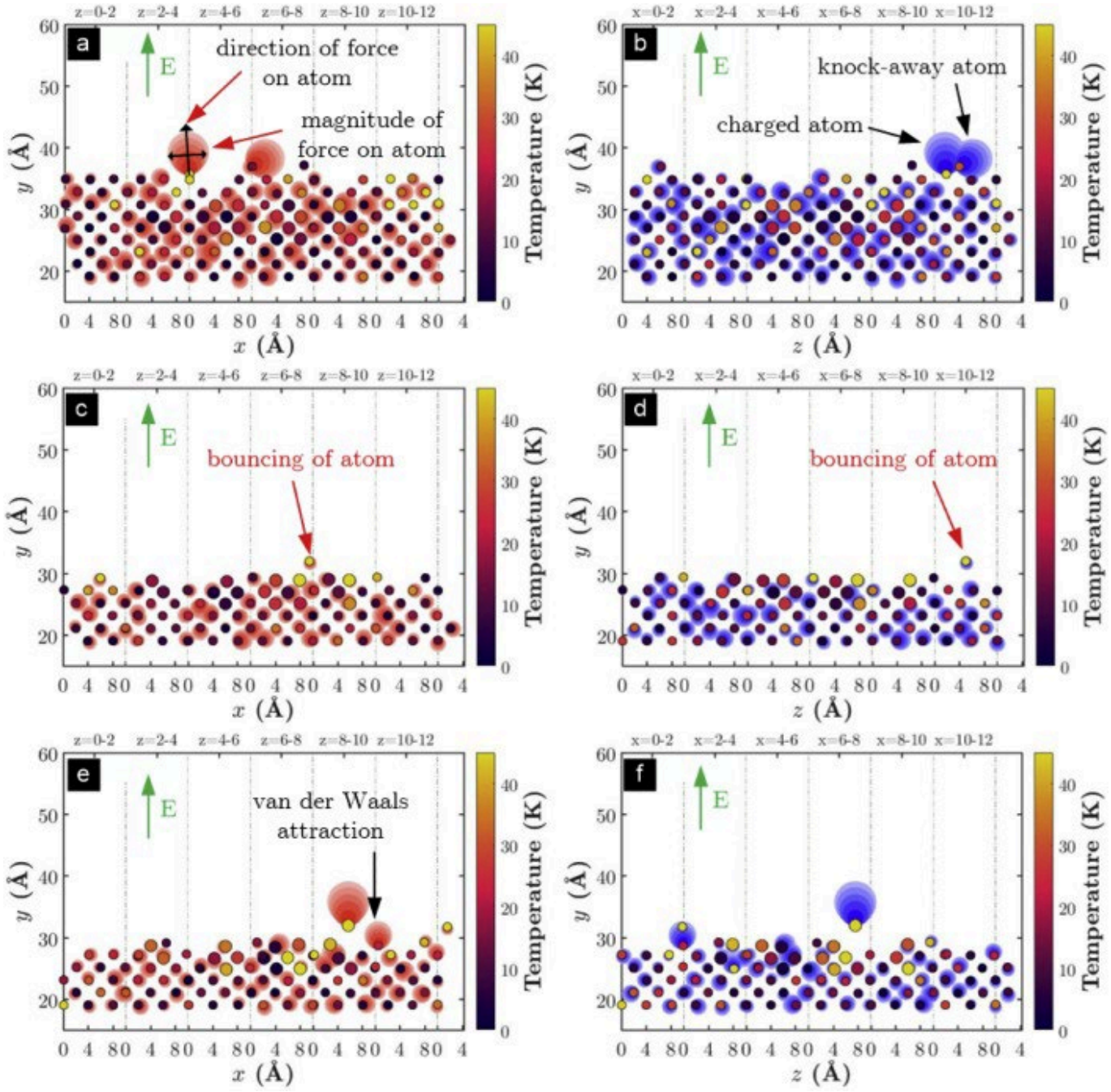

Fig. 3. (a) *x-y* view and (b) *z-y* view snapshots during a knock-away event between a charged atom and a non-charged atom, (c) *x-y* view and (d) *z-y* view snapshots during the bouncing of a non-charged atom, and (e) *x-y* view and (f) *z-y* view snapshots showing the van der Waals attraction between a charged atom and a non-charged atom. The small and large black-line circles indicate Al and Cr atoms, respectively, and the color in the circle indicates the temperature. Red and blue spread around atoms indicates the direction and magnitude of the force vector acting on those atoms, as demonstrated in a). (For interpretation of the references to color in this figure legend, the reader is referred to the web version of this article)

Fig. 4(a) shows the path of motion of atoms before they are ionized/charged. It is evident that the disturbance not only can cause a non-charged particle to be knocked and to bounce on the surface to another position but also may fully knock an atom away from the surface. The results show that the majority of collision events cause atoms to bounce on the surface, but a small portion (<10%) of collisions can knock atoms away from the surface.

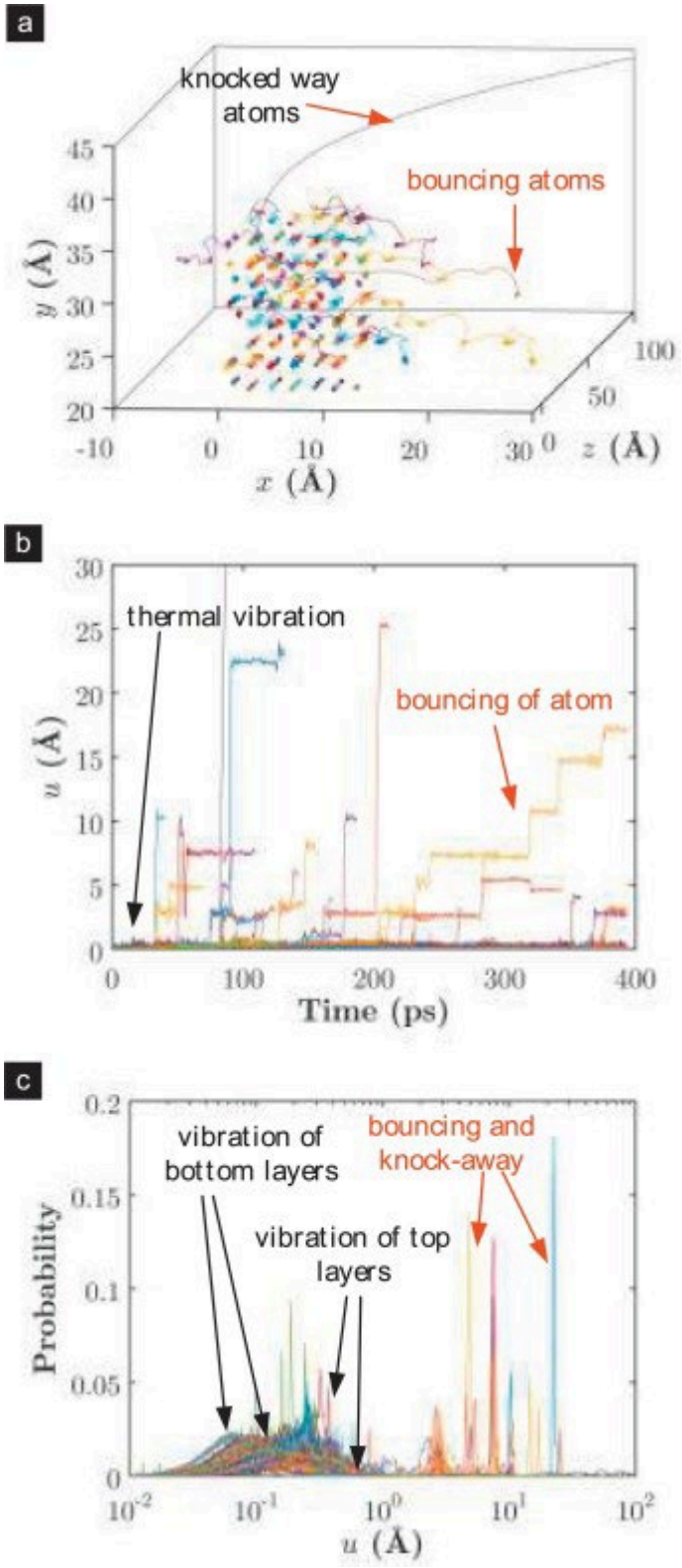

Fig. 4. (a) Motion path of atoms before ionization, (b) displacement of atoms from their original position over time, and c) probability distribution of atom displacement. In (a)-(c), one line is plotted for each atom.

The displacement of the atoms (181 atoms) from their original position, u, is plotted in Fig. 4(b) against time. It can be seen in that, among the 181 atoms, 24 have significantly increased displacement while the rest of the atoms vibrate with u close to zero. The increase in displacements is often stepwise, as shown in Fig. 4(b), indicating that a bouncing atom jumps to a new position, vibrates for a period of time, and then jumps to another position. The probability distributions of each atom in Fig. 4(b) also show that the thermal vibration of atoms and the bouncing or flying away of atoms manifest distinct peaks. It is found that thermal vibration of the atoms is unlikely to result in displacement greater than 1 Å. By matching the distribution curves in Fig. 4(c) with the atom positions in Fig. 4(a), it can be seen that the thermal vibration of the atoms in the bottom layers with smaller y manifests smaller displacement due to thermal vibration, a finding that is consistent with the observation in Fig. 3. Fig. 4(b) and (c) demonstrate that thermal vibration causes displacement (u) of less than 1 Å whereas bouncing of the atoms causes displacement in the range of 1–25 Å.

3.2. Disturbance to flight path

Besides the disturbance of atom positions, another source of error lies in the flight path of the atoms. The atoms are assumed to accelerate with a force of Eq in the direction of E which is perpendicular to the surface. Assuming that at time t_0 an electric field pulse of E is applied to ionize an atom, and at time t the atom is removed, the coordinate of the atom is x_t, y_t, and z_t and the original coordinate is x_0, y_0, and z_0, then the position of the atom can be calculated as

(3) $x_0 = x_t$

(4) $z_0 = z_t$

$$y_0 = y_t - \frac{Eq(t_t - t_0)^2}{2m} \quad (5)$$

where E is field strength, q is the charge of the atom, and m is the atom mass.

However, in the realistic evaporation process, the force can be affected by thermal vibration, van der Waals attraction, collision, and nearby charges, and therefore not equal to Eq. When the acceleration force is not equal to Eq, errors will be introduced to the predicted atom position. As shown in Fig. 5(a) and (b), differences can be seen between the predicted position (Fig. 5(b)) and the pre-ionized position of the atoms (Fig. 5(a)). In that case, the surface ion density is relatively low and therefore there is no effect of nearby charges. The predicted atomic position in Fig. 5(b) serves as a good representation of the layered lattice structure, with the position of the Cr core identifiable. The actual force components in the y and x/z directions on each ionized atom is plotted against travel distance of the atoms in the y direction in Fig. 5(c) and (d). Fig. 5(c) shows that the y direction force on the atom equals Eq when the travel distance is greater than 10 Å, except for one atom which collides with a knocked-away, non-charged atom at the travel distance ≈ 10–13 Å The van der Waals force is found to reduce F_y by up to about 3% while a collision can cause a reduction of up to about 25%. The collision also results in peaks in F_x or F_z with magnitude up to 0.9 Eq within a travel distance of 5 Å.

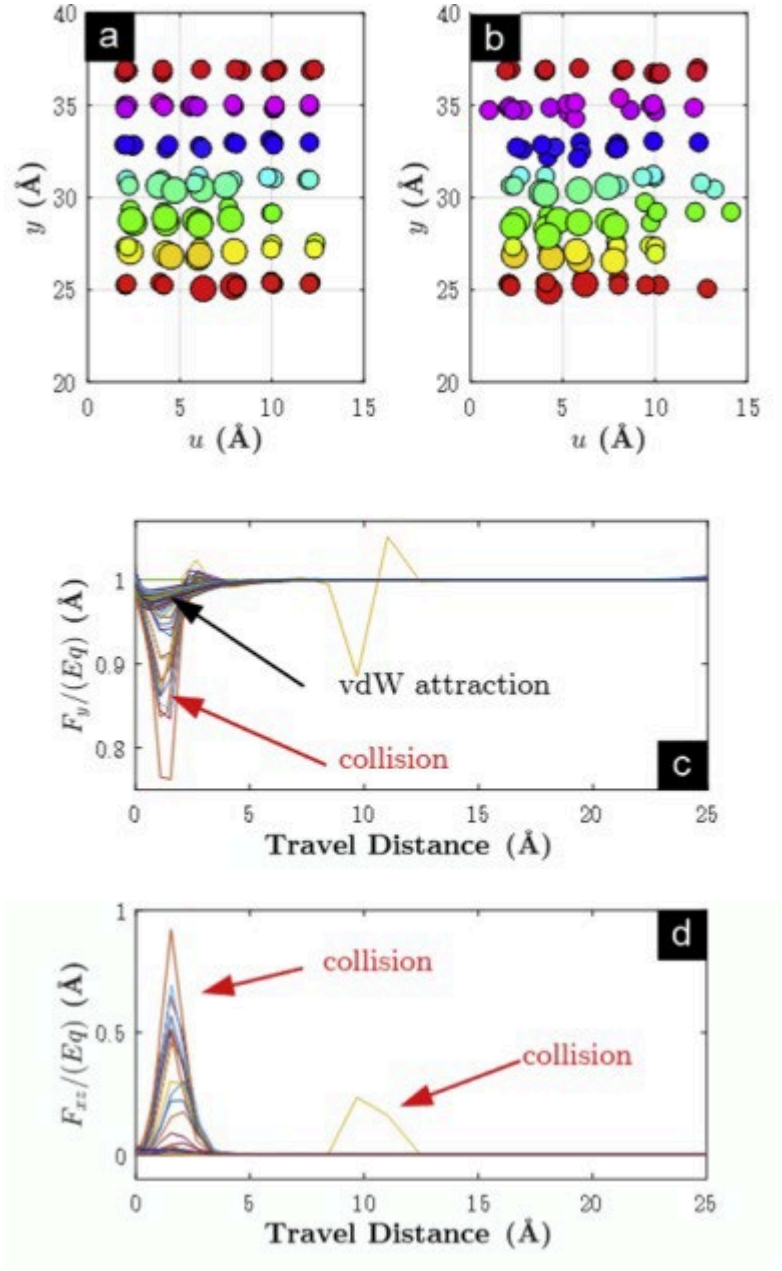

Fig. 5. (a) Position of atoms before ionization, (b) computed position of atoms based on Eqs. (3)–(5) and actual force acting on each ionized atom in the (c) y and (d) x or z direction, respectively, for $E = 136$ V/nm and surface ion density 1.2×10^{-4} e/nm^2.

However, when the material is atomically thin with very low surface roughness, such as the graphene shown in Fig. 1b, the friction caused by abrasion and wear is substantially reduced. MD simulations were conducted to evaluate the friction level between MLG and various matrices. In the example of the simulated system shown in Fig. 2a, the MLG has a sliding speed v_x and a sliding distance δ. Fig. 2b–d show the decrease of v_x during the sliding in different matrices from $\delta = 0$ to 10 Å due to friction. From Fig. 2b–d it can be seen that there is an initial sharper drop in v_x within 2 Å for each of the three different matrices and after that, the rate of decrease of v_x becomes relatively stable.

3.3. Effect of surface ion density and field strength

Based on the foregoing results and discussion, five objective functions are proposed, listed in Table 1, to quantify the APT error in the evaporation process. The ratio of collision events (ROC) is the ratio between the number of collision events and the number of ionized atoms. The average displacement, u(Å), is an objective function of the disturbance. The position error, P(Å), is used to indicate the degree of difference between the pre-ionized position and the predicted position which is calculated as

(6) $P_x = 0$

(7) $P_z = 0$

(8) $P_y = y_c - y_0$

where P_x, P_y, P_z is the component of the position error in the x, y, and z directions respectively, and y_c is the measured position of the atom when it is charged. The two force objective functions 'Average F_y/Eq' and 'Average F_{xz}/Eq' indicate the position prediction of error in the y direction and the x-z plane respectively. Simulations with different field strengths E and surface ion density were conducted. The values of the objective functions were computed and are listed in Table 1.

Table 1. Key objective functions.

σ (e/nm^2)	***E* (V/nm)**	**ROC**	***u*(Å)**	***P*(Å)**	**Average F_y/Eq**	**Average F_{xz}/Eq**
1.27×10^{-4}	85	0.10	0.354 ± 0.36	0.44 ± 0.45	1.00 ± 0.00	0.0064 ± 0.02
1.27×10^{-4}	102	0.09	0.22 ± 0.17	0.44 ± 0.52	0.99 ± 0.01	0.0062 ± 0.02
1.27×10^{-4}	119	0.14	0.31 ± 0.26	0.29 ± 0.31	0.99 ± 0.00	0.0036 ± 0.01
1.27×10^{-4}	136	0.17	0.471 ± 0.68	0.415 ± 0.58	0.99 ± 0.00	0.0088 ± 0.02
0.41	119	0.14	0.32 ± 0.32	1.63 ± 3.54	0.99 ± 0.01	0.011 ± 0.02
0.76	119	0.13	0.35 ± 0.31	3.87 ± 5.74	0.99 ± 0.11	0.024 ± 0.03
1.47	119	0.14	0.31 ± 0.281	9.05 ± 11.00	0.98 ± 0.17	0.049 ± 0.06
1.47	85	0.13	0.38 ± 0.33	8.02 ± 9.10	1.00 ± 0.08	0.064 ± 0.07
1.47	102	0.12	0.417 ± 0.41	10.31 ± 9.40	0.99 ± 0.26	0.043 ± 0.05
1.47	136	0.13	0.429 ± 0.412	9.61 ± 10.61	0.97 ± 0.19	0.062 ± 0.04

The surface ion density is an important parameter to consider in APT [1], as surface ion density can be affected by tip geometry and electric field strength [1]. The simulation results indicate that surface ion density may have a significant influence on APT accuracy. As demonstrated in Fig. 6, increased surface ion density may result in multiple adjacent atoms being ionized and evaporated together, with repulsion forces observed between these ions.

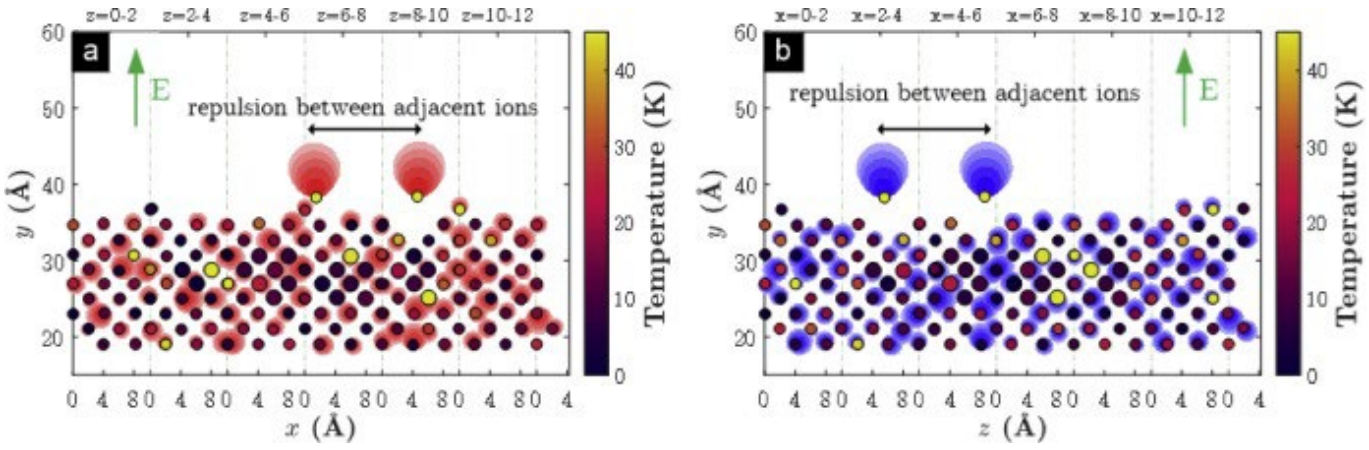

Fig. 6. (a) x-y view and (b) z-y view snapshots during the evaporation of atoms with surface ion density =0.76/nm^2. The small and large black-line circles indicate Al and Cr atoms, respectively; color in the circle indicates temperature. Red and blue spread around atoms indicate the direction and magnitude of the force vector acting on each atom, as demonstrated in a). (For interpretation of the references to color in this figure legend, the reader is referred to the web version of this article)

As a result, a large error is introduced to the back-calculated position of the atoms, as shown in Fig. 7(a) and (b). Fig. 7(a) and (b) demonstrate that at the surface ion density σ = 1.6 e/nm^2, the back-calculated position of

atoms can no longer represent the layer lattice structure and the position of the Cr core. Moreover, it is evident from Fig. 7(c) and (d) that F_y is biased from Eq for most of the atoms and F_{xz} is significantly different from zero throughout the travel distance 0–25 Å. This type of error is difficult to mitigate via improvement of the back-calculation model because the direction and magnitude of the force are subject to considerable randomness.

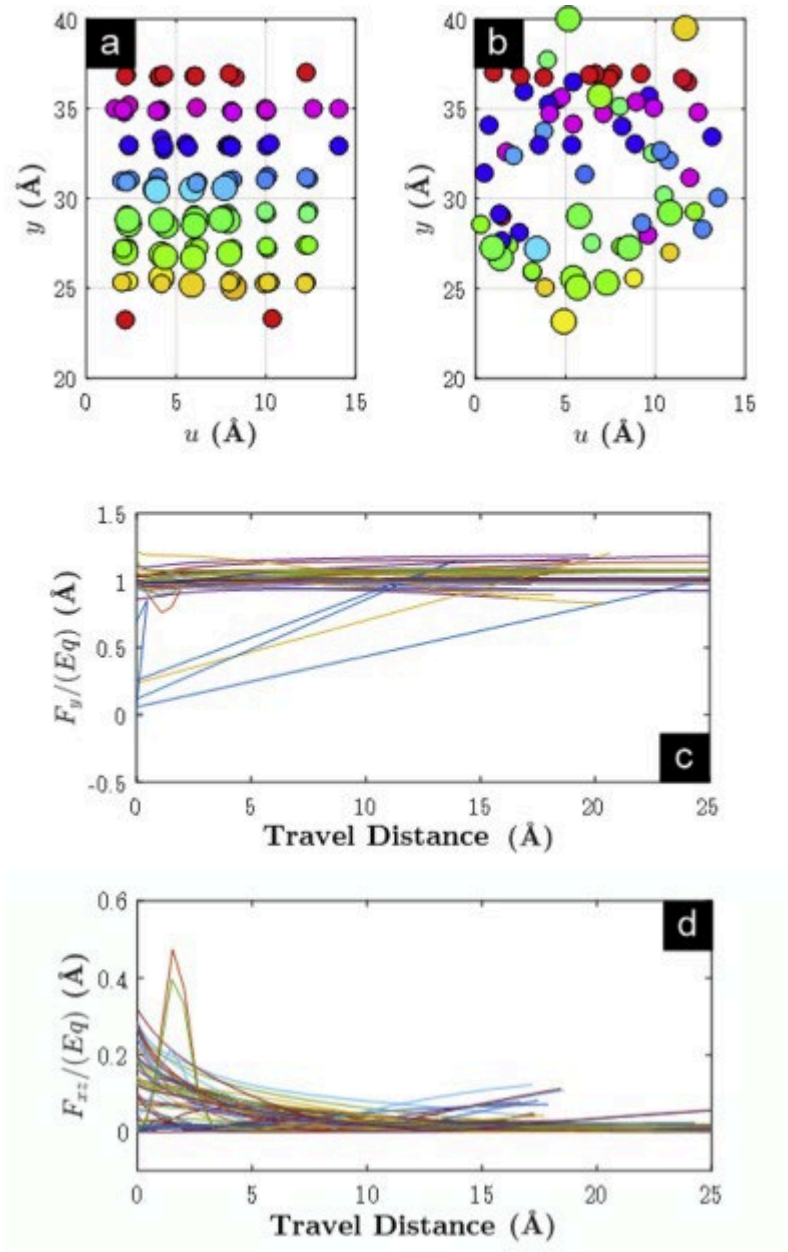

Fig. 7. (a) Position of atoms before ionization, (b) computed position of atoms based on Eq (3)–(5) and actual force acting on each ionized atom in the (c) y and (d) x or z directions, respectively, for $E = 136$ V/nm and surface ion density 1.5 e/nm^2.

Fig. 8(a)–(c) shows the effect of surface ion density on displacement, position errors of F_y and F_{xz}. Fig. 8(a) shows that when $E = 119$ V/nm, the average displacement fluctuates at about 0.3 Å, showing the insignificant effect of the surface ion density. The position error, however, increases significantly with σ from less than 1 Å to about 10 Å. A similar trend is observed on F_y/Eq and F_{xz}/Eq, in that when σ increases, stronger repulsion between ions reduces F_y while increasing F_{xz}. These results suggest that the surface ion density needs to be controlled to about 0.2–0.3 e/nm^2 in order to minimize the error in evaporation and the time or number of pulses [6] required to evaporate sufficient material from the specimen tip.

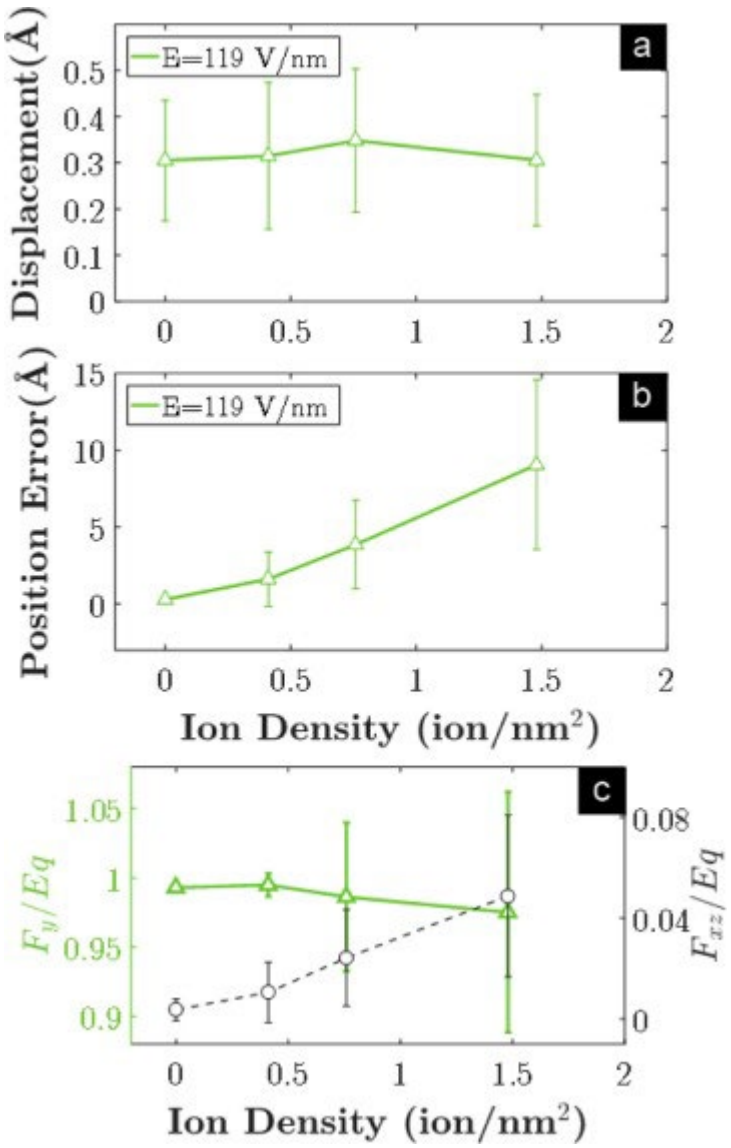

Fig. 8. Effect of ion density on (a) average displacement, (b) position error, (c) average F_y and average F_{xz}. Error bar indicates 0.5 standard deviation.

Fig. 9 shows the effect of field strength E on displacement and position error of F_y. Fig. 9(b) shows that field strength has less effect on position errors compared to the effect of ion density. The magnitude of the average position error varies within about 25% for both $\sigma = 1.2 \times 10^{-4}$ e/nm^2 and 1.5 e/nm^2. For displacement and F_y, the effect of field strength demonstrates dependence on the surface ion density. Fig. 9(a) shows that the disturbance to the atom structure is more sensitive to field strength when the atoms are evaporated one by one ($\sigma = 1.2 \times 10^{-4}$ e/nm^2). The results show that when the optimum field strength is about 110 V/nm for $\sigma = 1.2 \times 10^{-4}$ e/nm^2 and 85 V/nm for $\sigma = 1.5$ e/nm^2, the total average error generated during the evaporation process is calculated as the sum of the average displacement and position error, assuming that these two are independent variables [46]. For low surface ion density (about 0.0001–0.3 e/nm2), the total average error is about 1–2 Å, which is close to the experimentally measured reconstruction error (about 1 Å) [47]. These results also demonstrate that, besides commonly recognised errors during the flight process [1], [30], [47], the evaporation process is an important source of error in the reconstruction. In experiments, researchers often need to optimize parameters such as field strength [21], [22], [47] and number of atoms detected per hour [47]. The results and approaches presented in this study can be utilised to optimize these parameters and understand their effects.

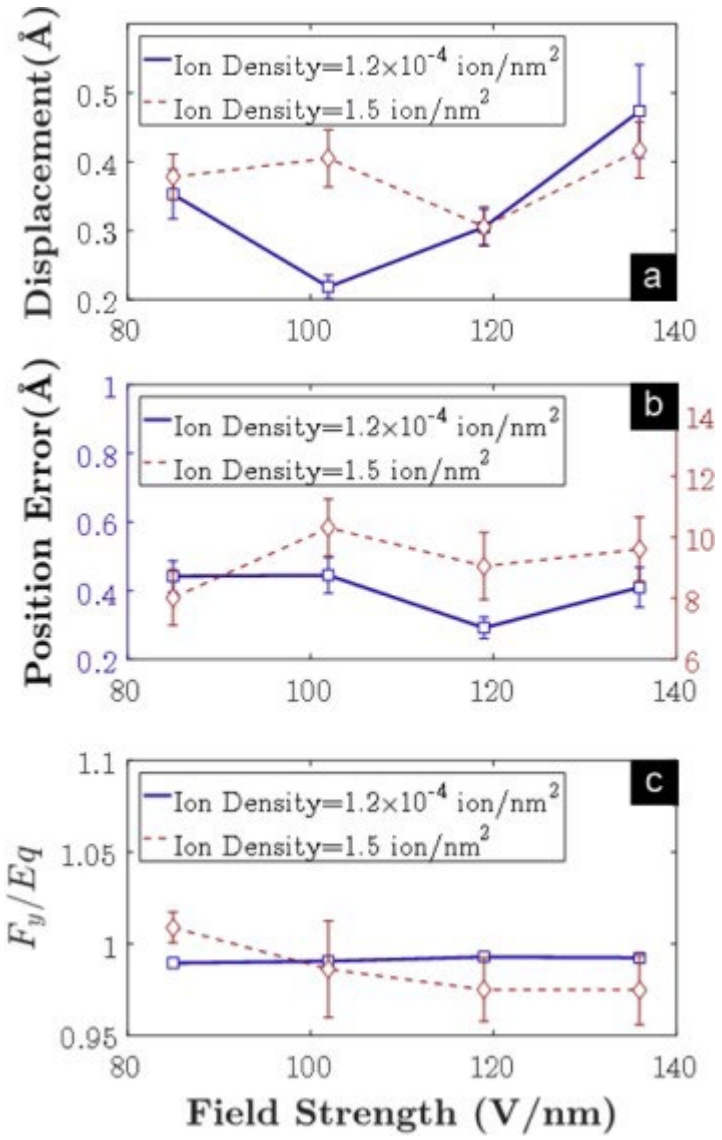

Fig. 9. Effect of field strength on (a) average displacement, (b) position error, (c) average F_y and average F_{xz}. Error bar indicates 0.1 standard deviation.

4. Conclusions

The present study used non-equilibrium MD simulation to study the movement of evaporated atoms on an atom probe surface. The results prove that the thermal vibration and collision between atoms can create disturbance in the position of atoms. It is found that thermal vibration causes up to 1 Å displacement of atoms and collisions cause displacement from 1 to 25 Å. The average atom displacements from different simulated cases are found to vary between 0.2 to 0.5 Å. Collision and repulsion between evaporated atoms demonstrate significant effects on the flight path of atoms within 15 Å from the surface. Collision is found to affect about 9 to 17% of atoms, resulting in errors in the back-calculated positions of atoms. The average error in the back-calculated positions of atoms is 0.3–0.5 Å when the density of evaporated atoms per pulse is minimal, but it can increase to 8–10 Å when more than 1.5 e/nm^2 atoms are evaporated per pulse. It is suggested that surface ion density should be controlled below 0.2–0.3 e/nm^2 to minimize errors in the evaporation process.

Acknowledgements

The authors are grateful for the financial support of the Australian Research Council in conducting this study.

References

[1] T. Li, P.A. Bagot, E.A. Marquis, S.E. Tsang, G.D. Smith, Characterization of oxida- tion and reduction of Pt–Ru and Pt–Rh–Ru alloys by atom probe tomography and comparison with Pt–Rh, J. Phys. Chem. C 116 (2012) 17633–17640.

[2] R. Agrawal, R.A. Bernal, D. Isheim, H.D. Espinosa, Characterizing atomic com- position and dopant distribution in wide band gap semiconductor nanowires using laser-assisted atom probe tomography, J. Phys. Chem. C 115 (2011) 17688–17694.

[3] K. Thompson, D. Lawrence, D. Larson, J. Olson, T. Kelly, B. Gorman, In situ site-specific specimen

preparation for atom probe tomography, Ultrami- croscopy 107 (2007) 131–139.
[4] D. Isheim, R.P. Kolli, M.E. Fine, D.N. Seidman, An atom-probe tomographic study of the temporal evolution of the nanostructure of Fe–Cu based high--strength low-carbon steels, Scr. materialia 55 (2006) 35–40.
[5] D.N. Seidman, Three-dimensional atom-probe tomography: advances and ap- plications, Annu. Rev. Mater. Res. 37 (2007) 127–158.
[6] F. De Geuser, B. Gault, A. Bostel, F. Vurpillot, Correlated field evaporation as seen by atom probe tomography, Surf. Sci. 601 (2007) 536–543.
[7] D. Blavette, A. Bostel, J. Sarrau, B. Deconihout, A. Menand, An atom probe for three-dimensional tomography, Nature 363 (1993) 432–435.
[8] E. Cadel, F. Vurpillot, R. Lardé, S. Duguay, B. Deconihout, Depth resolution func- tion of the laser assisted tomographic atom probe in the investigation of semi- conductors, J. Appl. Phys. 106 (2009) 044908.
[9] B. Gault, M.P. Moody, F. De Geuser, A. La Fontaine, L.T. Stephenson, D. Haley, S.P. Ringer, Spatial resolution in atom probe tomography, Microsc. Microanal. 16 (2010) 99–110.
[10] T.F. Kelly, M.K. Miller, Atom probe tomography, Rev. Sci. Instrum. 78 (2007) 031101.
[11] T. Li, P.A. Bagot, E.A. Marquis, S.E. Tsang, G.D. Smith, Characterization of oxida- tion and reduction of a palladium–rhodium alloy by atom-probe tomography, J. Phys. Chem. C 116 (2012) 4760–4766.
[12] J.R. Riley, D.E. Perea, L. He, F. Tsui, L.J. Lauhon, Correlation and morphology of dopant decomposition in Mn and Co codoped Ge epitaxial films, J. Phys. Chem. C 116 (2011) 276–280.
[13] Y. Chen, T. Ohkubo, M. Kodzuka, K. Morita, K. Hono, Laser-assisted atom probe analysis of zirconia/spinel nanocomposite ceramics, Scr. Materialia 61 (2009) 693–696.
[14] M. Thuvander, J. Weidow, J. Angseryd, L.K. Falk, F. Liu, M. Sonestedt, K. Stiller, H.-O. Andrén, Quantitative atom probe analysis of carbides, Ultramicroscopy 111 (2011) 604–608.
[15] K. Nomoto, H. Sugimoto, A. Breen, A.V. Ceguerra, T. Kanno, S.P. Ringer, I.P. Wurfl, G. Conibeer, M. Fujii, Atom probe tomography analysis of Boron and/or Phosphorus distribution in doped Silicon nanocrystals, J. Phys. Chem. C 120 (2016) 17845–17852.
[16] O. Nishikawa, H. Kato, Atom-probe study of a conducting polymer: the oxida- tion of polypyrrole, J Chem. Phys. 85 (1986) 6758–6764.
[17] T. Prosa, S. Kostrna, T. Kelly, Laser atom probe tomography: application to poly- mers, in: 2006 19th International Vacuum Nanoelectronics Conference, IEEE, 2006, pp. 533–534.
[18] T.F. Kelly, O. Nishikawa, J.A. Panitz, T.J. Prosa, Prospects for nanobiology with atom-probe tomography, MRS Bull. 34 (2009) 744–750.
[19] L.M. Gordon, D. Joester, Nanoscale chemical tomography of buried organic-i- norganic interfaces in the chiton tooth, Nature 469 (2011) 194–197.
[20] T. Tsong, Field ion image formation, Surf. Sci. 70 (1978) 211–233.
[21] T.T. Tsong, Atom-Probe Field Ion Microscopy: Field Ion Emission, and Surfaces and Interfaces at Atomic Resolution, Cambridge University Press, 2005.
[22] L. Tseng, J. Ma, B. Hornbuckle, I. Karaman, G. Thompson, Z. Luo, Y. Chumlyakov, The effect of precipitates on the superelastic response of [100]oriented FeM- nAlNi single crystals under compression, Acta Materialia 97 (2015) 234–244.
[23] B. Hornbuckle, T. Sasaki, G. Bigelow, R. Noebe, M. Weaver, G. Thompson, Struc- ture–property relationships in a precipitation strengthened Ni–29.7 Ti–20Hf (at%) shape memory alloy, Mater. Sci. Eng. 637 (2015) 63–69.
[24] H.S. Hasting, A.G. Frøseth, S.J. Andersen, R. Vissers, J.C. Walmsley, C.D. Mar-ioara, F. Danoix, W. Lefebvre, R. Holmestad, Composition of β rrprecipitates in Al–Mg–Si alloys by atom probe tomography and first principles calculations, J. Appl. Phys. 106 (2009) 123527.
[25] K. Hono, T. Ohkubo, Y. Chen, M. Kodzuka, K. Oh-Ishi, H. Sepehri-Amin, F. Li, T. Kinno, S. Tomiya, Y. Kanitani, Broadening the applications of the atom probe technique by ultraviolet femtosecond laser, Ultramicroscopy 111 (2011) 576–583.
[26] R. Schlesiger, C. Oberdorfer, R. Würz, G. Greiwe, P. Stender, M. Artmeier, P. Pelka, F. Spaleck, G. Schmitz, Design of a laser-assisted tomographic atom probe at Münster University, Rev. Sci. Instrum. 81 (2010) 043703.
[27] E.A. Marquis, N.A. Yahya, D.J. Larson, M.K. Miller, R.I. Todd, Probing the im- probable: imaging C atoms in alumina, Mater. Today 13 (2010) 34–36.
[28] B. Gault, F. De Geuser, L.T. Stephenson, M.P. Moody, B.C. Muddle, S.P. Ringer, Estimation of the reconstruction parameters for atom probe tomography, Mi- crosc. Microanal. 14 (2008) 296–305.
[29] C. Oberdorfer, G. Schmitz, On the field evaporation behavior of dielectric ma- terials in three-dimensional atom probe: a numeric simulation, Microsc. Mi- croanal. 17 (2011) 15–25.
[30] E.P. Silaeva, M. Karahka, H. Kreuzer, Atom probe tomography and field evap- oration of insulators and semiconductors: theoretical issues, Curr. Opin. Solid State Mater. Sci. 17 (2013) 211–216.
[31] B. Gault, F. Vurpillot, A. Vella, M. Gilbert, A. Menand, D. Blavette, B. Deconi- hout, Design of a femtosecond laser assisted tomographic atom probe, Rev. Sci. Instrum. 77 (2006) 043705.
[32] A. McLachlan, Van der Waals forces between an atom and a surface, Mol. Phys. 7 (1964) 381–388.
[33] G. Binnig, C.F. Quate, C. Gerber, Atomic force microscope, Phys. Rev. lett. 56 (1986) 930.
[34] H. Heinz, R. Vaia, B. Farmer, R. Naik, Accurate simulation of surfaces and in- terfaces of face-centered cubic metals using 12− 6 and 9− 6 Lennard-Jones potentials, J. Phys. Chem. C 112 (2008) 17281–17290.

[35] B.J. Garrison, E.J. Dawnkaski, Molecular dynamics simulations of dimer opening on a diamond (001)(2x1) surface, Science 255 (1992) 835.
[36] W. Hoover, Nonequilibrium molecular dynamics, Annu. Rev. Phys. Chem. 34 (1983) 103–127.
[37] F. Seitz, On the theory of diffusion in metals, Acta Crystallogr. 3 (1950) 355–363.
[38] D. Blavette, B. Deconihout, A. Bostel, J. Sarrau, M. Bouet, A. Menand, The tomo- graphic atom probe: a quantitative three-dimensional nanoanalytical instru- ment on an atomic scale, Rev. Sci. Instrum. 64 (1993) 2911–2919.
[39] J. Takahashi, K. Kawakami, Y. Kobayashi, T. Tarui, The first direct observation of hydrogen trapping sites in TiC precipitation-hardening steel through atom probe tomography, Scripta Materialia 63 (2010) 261–264.
[40] H. Sun, COMPASS: an ab initio force-field optimized for condensed-phase ap- plications overview with details on alkane and benzene compounds, J. Phys. Chem. B 102 (1998) 7338–7364.
[41] D. Rigby, H. Sun, B. Eichinger, Computer simulations of poly (ethylene ox- ide): force field, pvt diagram and cyclization behaviour, Polym. Int. 44 (1997) 311–330.
[42] A. Ortega-Rodriguez, F. Alvarez-Ramirez, S. Cruz, C. Lira-Galeana, A model to calculate the average interaction energy and adhesion force between petroleum asphaltenes and some metallic surfaces, J. Colloid Interface Sci. 301 (2006) 352–359.
[43] K. Khaled, Electrochemical investigation and modeling of corrosion inhibition of aluminum in molar nitric acid using some sulphur-containing amines, Cor- rosion Sci. 52 (2010) 2905–2916.
[44] H. Margenau, Van der Waals forces, Rev. Mod. Phys. 11 (1939) 1.
[45] C.C. Heyde, E. Seneta, IJ Bienaymé: statistical theory anticipated, Springer Sci- ence & Business Media, 2012.
[46] D. Larson, B. Geiser, T. Prosa, S. Gerstl, D. Reinhard, T. Kelly, Improvements in planar feature reconstructions in atom probe tomography, J. Microsc. 243 (2011) 15–30.